Protein Crowding mediates Passive Membrane Remodeling in ESCRT-induced Formation of Intraluminal Vesicles

Susanne Liese[1], Eva Maria Wenzel[2], Rossana V. Rojas Molina[1], Sebastian W. Schultz[2], Harald Stenmark[2], Camilla Raiborg[2], and Andreas Carlson[1*]

[1]Department of Mathematics, Mechanics Division, University of Oslo, Oslo, Norway
[2]Department of Molecular Cell Biology, Institute for Cancer Research, Oslo University Hospital, Montebello, N-0379, Oslo, Norway
[*]Email: acarlson@math.uio.no

Abstract

As part of the lyosomal degradation pathway, the endosomal sorting complex required for transport (ESCRT) machinery sequester receptors at the endosome and simultaneously deform the membrane to generate intraluminal vesicles (ILVs). The role ESCRTs play in the membrane shape remodeling is not understood. We present a mathematical model, where ESCRT-induced alteration of the Gaussian bending rigidity and their crowding on the membrane facilitate ILV formation. The combination of mathematical modeling and experimental measurements shows that early ESCRT-driven budding does not require ATP consumption as only a small energy barrier needs to be overcome. Our model predicts that an ESCRT-free ILV forms, *i.e.*, ESCRTs do not become part of the vesicle, but localize with a high density at the membrane neck, where the steep decline in the Gaussian curvature might trigger ESCRT-III/Vps4 assembly to enable neck constriction and scission.

Introduction

Sorting and compartmentalisation of biomaterials lie at the heart of cellular processes and plays a fundamental role in the lysosomal degradation pathway to regulate cellular activities. Transmembrane proteins in the plasma membrane, such as growth factor receptors, are internalized by endocytosis and degraded in lysosomes [1, 2]. As a part of this pathway, intraluminal vesicles (ILVs) with a typical diameter in the order of 50nm are formed inside endosomes [3]. The ILV formation starts with a small deformation of the endosome membrane, which grows over time and finally leads to a cargo-containing vesicle within the endosome lumen. ILVs are an essential part of the endocytic downregulation of activated receptors to ensure signal attenuation, failure of which results in tumourigenic signaling [3, 4, 5, 6]. In addition, ILVs can reach the extracellular environment as exosomes, where they become signaling entities enabling intercellular communication. Altered exosomes can serve as tumor biomarkers [7, 8, 9]. In spite of the fundamental role ILVs play in the endocytic pathway, surprisingly little is known about the mechanochemical crosstalk that regulates their formation [10].

The biophysical process that leads to the formation of an ILV is in many ways inverse to clathrin-mediated endocytosis at the plasma membrane, as the membrane bud protrudes away from the cytosol (Fig. 1a) and the vesicle shape is not dictated by a protein scaffold [4]. Cargo sorting and ILV formation is mediated by the endosomal sorting complex required for transport (ESCRT) [11, 12, 5, 13, 14], which consists of four sub-complexes, ESCRT-0, -I, -II and - III, and the accessory Vps4 complex. Each of the sub-complexes have different, yet complementary tasks [5, 14]. ESCRT-0 contains binding domains for the endosome membrane, ubiquinated cargo and clathrin [5], which enables ESCRT-0 to sequester cargo material into patches, so-called microdomains, on the endosome membrane. Interestingly, the role clathrin plays in ILV formation differs significantly from its role in endocytosis, as it promotes ILV formation [15], but does not form a basket-like scaffold. Instead, a rather flat clathrin coat is bound to the ESCRT microdomain [16, 17, 18, 1]. ESCRT-0 recruits ESCRT-I that leads to the recruitment of the complete ESCRT machinery. While ESCRT-0, -I, -II sequester transmembrane cargo proteins and facilitate ILV formation, ESCRT-III and the ATPase Vps4 enable constriction of the membrane neck leading to the formation of an ILV [19]. Notably, the only energy consuming step in the membrane remodeling process is the membrane scission, involving the ATPase Vps4 [20, 21]. This is especially remarkable, since the energy required for a flat lipid bilayer to form a spherical vesicle, is several orders of magnitude larger than the thermal energy, thus creating an energy barrier inhibiting vesicle formation [22, 23].

Experiments have shown that the recruitment of ESCRTs to the endosome occur in a time periodic fashion [15, 24], where each recruitment cycle is associated with the formation of a single ILV. Transmission electron microscopy (TEM) images have also provided a high-level description of the membrane shapes during the budding process [15]. Today, *in-vivo* measurement techniques are not able to record the time evolution of fluorescent markers and the membrane shape simultaneously. To gain a detailed understanding of ESCRT assembly on the endosome membrane giant unilaminar vesicles (GUV) have been used as an *in-vitro* model system to study the formation of micrometer sized vesicles at their membrane [13]. The *in-vitro* experiments demonstrate that ESCRTs are enriched in the vesicle neck but do not coat the main portion of the vesicle [13].

Among the ESCRT sub-complexes, ESCRT-III and Vps4 have received most attention in both experimental and theoretical studies, due to their fundamental role in a broad range of cellular processes involving membrane scission, e.g., cytokinesis and virus budding [25, 19, 26, 27, 28, 29, 30, 31, 32, 33, 34]. Theoretical and experimental studies have shown that the polymerization of ESCRT-III filaments into spirals promotes membrane buckling [35] and neck scaffolding [36], which in combination with the tension exerted by ESCRT-III, is suggested to cause closure of the membrane neck [37]. Much less is known about how the early ESCRTs affect membrane-remodeling, even though they play an as critical role in ILV formation [15, 38, 39, 40]. The lack of a description of the biophysical mechanisms generating membrane deformations at the endosome contrasts the large number of studies on clathrin mediated endocytosis at the plasma membrane, with similar membrane shapes, where theoretical modeling has provided invaluable information about the link between surface forces from transmembrane proteins [41], stochastic effects [42] and the resistive elastic forces [43, 44, 45, 46]. To observe ILV formation Rozycki et al. [39] assumed a uniform ESCRT coat on the membrane, which exhibits preferred binding to negative Gaussian curvature. Mercker et al. considered the influence of a spontaneous Gaussian curvature caused by the structure of the ESCRT-I and ESCRT-II supercomplex . These models highlight that Gaussian bending is essential to understand the formation of an ILV.

In order to understand the underlying biophysical mechanisms of the ILV budding process driven by ESCRTs, we address the following questions:

1. What is the biomechanical mechanism that allows ILVs to form and does this process require an active force or an external energy?
2. How do ESCRT proteins organize at the endosome to form an ESCRT-free vesicle?
3. How do the dynamics of ESCRT recruitment couple to the endosome membrane shape?

To answer these fundamental questions, we combine theoretical modeling and experimental measurements, where we will show that ILV formation is facilitated by the ESCRT proteins' ability to alter the Gaussian bending rigidity and their crowding on the membrane.

Results

Experimental measurements: We start by describing the dynamics of ESCRT assembly on the endosome, which was recently measured experimentally [15]. Fluorescence measurements of ESCRT-proteins dynamics were performed by live-cell microscopy of human cancer cells (HeLa), which show that ILV formation is accompanied by an oscillatory increase and decrease of the ESCRT concentration on the limiting membrane of endosomes [15], as illustrated in Fig.1b. In each recruitment cycle, the fluorescent signal of ESCRT-0 continuously increases over a time span of about three minutes, before it abruptly starts to decrease for about two minutes. In addition, it was shown that ESCRT-I and clathrin have similar dynamics as ESCRT-0. We therefore only need to consider the temporal evolution of ESCRT-0. The dynamic features of ESCRT-III are distinctly different from the ESCRT subunits 0-I. Once the ESCRT-0 signal reaches a maximum in fluorescence intensity, ESCRT-III exhibits a jump in its fluorescence intensity over just a few seconds, before it decreases with a decay time similar to ESCRT-0. The dynamics of ESCRT assembly are described by two time scales: the dwell time of ESCRT-0 τ_{d}=(161±94)s and the periodicity of the ESCRT-recruitment cycle, or equivalently the mean waiting time τ_{wt} =(203±47)s [15].

TEM imaging of HeLa cancer cells reveal that ILVs have an average diameter of ≈46nm and there is no apparent trend with respect to the endosome size, see Fig. 1c. A description of the membrane remodeling process that leads to ILV formation must therefore include a mechanism that is robust in terms of setting the vesicle diameter. TEM imaging also allows us to describe the membrane shape at different stages, where we categorize [15] the membrane profiles into three specific shapes: pit-, U- and Ω-shape (Fig.1 d, e). As there is no overweight of samples in either of these categories, despite that these images are taken for different cells and at random time points within the ILV formation cycle, it suggests that the membrane deformation takes place in a continuous rather than a jump-like fashion over time.

Energy barrier: Next, we use the fluorescent signal data from the experiments to extract information about the energy barrier that has to be overcome as an ILV forms. The magnitude of the energy barrier is crucial to classify whether ILV budding happens passively, *i.e.*, initiated by thermal fluctuations, or as an active processes that requires energy consumption. Kim et al. [47] derived a theory that relates the height of an energy barrier in a diffusive process to the ratio of the characteristic time scales $\tau_{\mathrm{d}}/\tau_{\mathrm{wt}}$. We deploy this theory for an energy landscape with the shape of an harmonic potential, which for an energy barrier ΔE_{B} predicts the two times scales; $\tau_{\mathrm{d}} \sim (4/3 - 16/45\beta\Delta E_{\mathrm{B}})\beta\Delta E_{\mathrm{B}}$ and $\tau_{\mathrm{wt}} \sim \pi\mathrm{erf}(\sqrt{\beta\Delta \mathrm{E_B}})\mathrm{erfi}(\sqrt{\beta\Delta \mathrm{E_B}})$, with β^{-1} the thermal energy. The ratio of the two experimental time scales, *i.e.*, the dwell time τ_{d} and the mean waiting time τ_{wt}, provides an upper limit for the magnitude of the energy barrier $\Delta E_{\mathrm{B}} \lessapprox 0.6\mathrm{k_B T}$ (see Supplementary information). Since ΔE_{B} is of such low magnitude, it can be overcome by thermal fluctuations, giving us a first suggestion that ILV budding happens as a passive process as we will further demonstrate by our theoretical model.

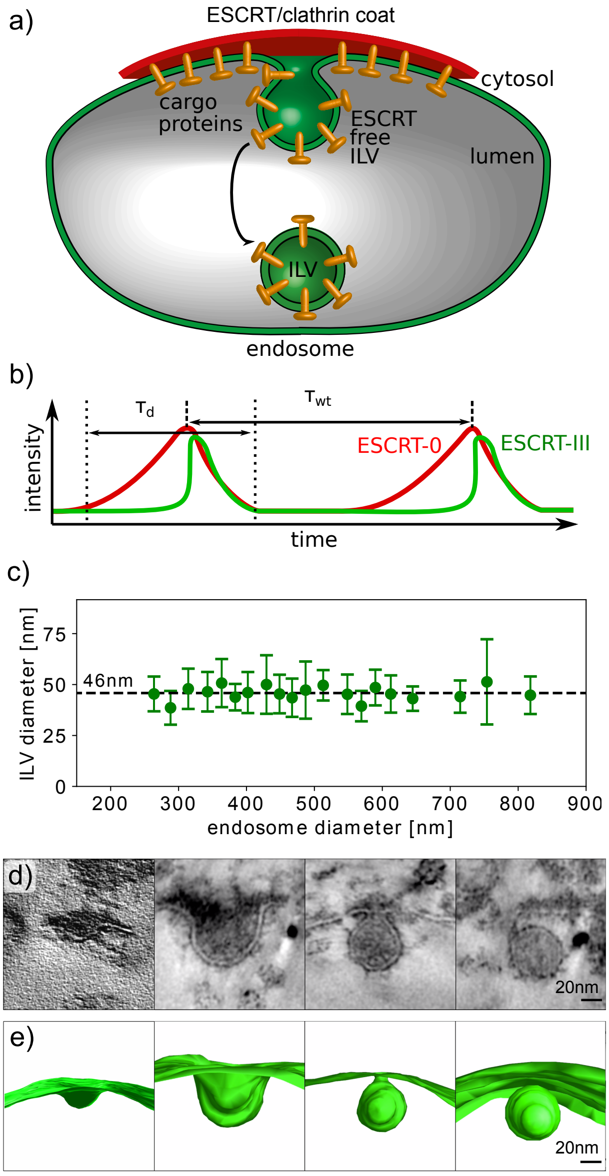

Figure 1: Illustration of the formation of ILVs: a) Schematic illustration of the formation of an ESCRT-free ILV. Transmembrane cargo proteins, ESCRTs and clathrin form a microdomain at the endosome, where cargo proteins are sorted by the ESCRT machinery into ILVs. b) We illustrate the characteristic time scales from the measured fluorescence intensity of ESCRT-0 and ESCRT-III [15]. The concentration increases and decreases again during the dwell time τ_{d}. The mean waiting time between two consecutive ILV formation events is denoted by τ_{wt}. c) Experimental measurement of 477 ILV diameters in HeLa cell endosomes exhibit a narrow distribution of ILV size independent of the endosome diameter. The ILV diameter was measured in TEM images. The average and the standard deviation are calculated over at least 10 ILV diameters. The endosome diameter is sorted into bins with a width of 20nm, the center of the bins is chosen such that the number of data points in each bin is maximized. d) During ILV formation the endosome membrane transitions through intermediate membrane shapes, illustrated by the TEM micrographes and classified (from left to right) into pit-shape, U-shape, Ω-shape and abscised vesicle [15]. e) We reconstruct the three dimensional membrane shapes, from TEM tomograms [15] (Supplementary Video 1). Subfigure d) and e) modified from [15]

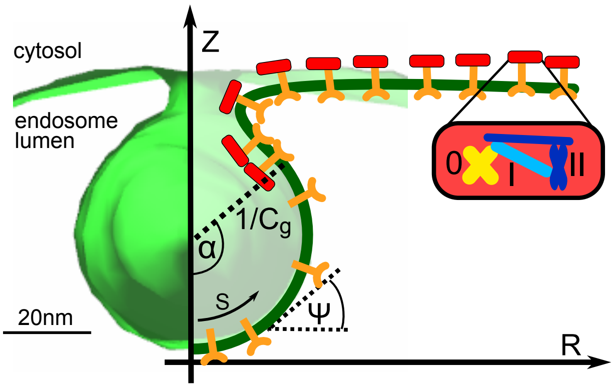

Figure 2: ILV parameterization: A part of the endosome membrane reconstructed from TEM micrographs (in green) is shown together with the parametrization of the membrane in the mathematical model. Membrane bound coat proteins (red blocks), which include ESCRT-0, -I, -II and clathrin, bind to the transmembrane proteins (Y-shaped orange markers). The endosome membrane deforms into an ESCRT-free spherical vesicle with a curvature $C_{\rm g}$, surrounded by a neck region with an elevated ESCRT density. The extent of the coat-free area is quantified by the opening angel α. The membrane shape is defined by the arc length S and the azimuthal angle ψ, where we treat the membrane as being axially symmetric around the Z-axis.

Mathematical model: A mathematical model that describes ILV formation needs to incorporate how ESCRT proteins influence the shape of the endosome membrane. We consider ESCRT-0, -I, -II and clathrin as one effective complex that coats the endosome membrane (Fig. 2), and the membrane together with the embedded cargo proteins is treated as a homogenous elastic surface. Since the ILV size is much smaller than both the endosome (see Fig. 1c and Supplementary Figure S1) and the ESCRT microdomain (several hundred nano meters in diameter) [15], we simplify the model by considering only a part of the endosome membrane that is approximately planar (Fig. 2), where cargo proteins are evenly distributed within the domain. As part of the budding process a region within the ESCRT microdomain forms that is not coated by ESCRTs [13], which we define as the ESCRT-free region (Fig. 2). TEM tomography experiments show that ILVs are very close to being rotationally symmetric (Supplementary Video 1 and 2), which we adopt in the mathematical model, where the membrane is determined by the arc length S and the azimuthal angle ψ (Fig. 2). The Z coordinate and the radial coordinate R of the membrane contour are related to S and ψ through $\frac{dZ}{dS} = \sin\psi$, $\frac{dR}{dS} = \cos\psi$. ILV formation involves a change in both mean and Gaussian curvature (see Supplementary information). A common feature among proteins that alter the Gaussian bending rigidity are α-helix motives in their secondary structure [48, 49, 50, 51, 52]. The structural similarity between these proteins and the ESCRTs prompts us to model the Gaussian bending rigidity as dependent on the concentration of ESCRT proteins. The simplest mathematical description of a protein-induced Gaussian bending rigidity is to assume a linear response with respect to the ESCRT density ρ. The Gaussian bending energy $\Delta E_{\rm g}$ then reads

$$\Delta E_{\rm g} = 2\pi \int_0^\infty \rho \gamma_{\rm g} C_1 C_2 R dS, \tag{1}$$

with the proportionality factor $\gamma_{\rm g}$. The principle curvatures of the membrane are denoted as $C_1 = \sin\psi/R$ and $C_2 = d\psi/dS$. In qualitative terms, a non-homogenous Gaussian bending rigidity describes the tendency of the membrane to deform into a neck-like shape.

In addition to $\Delta E_{\rm g}$, the total membrane energy has to account for membrane bending and stretching as well as protein crowding. By following the Helfrich model for lipid bilayers [22], we describe the membrane together with the embedded cargo proteins as a thin elastic sheet. The bending energy ΔE_κ is then obtained as an integral of the squared mean curvature over the entire surface

$$\Delta E_\kappa = 2\pi \int_0^\infty \frac{\kappa}{2} R \left(C_1 + C_2\right)^2 dS, \tag{2}$$

with the bending rigidity κ.

In the limit of an endosome that is much larger than the ILV, as is the case in this system, the pressure that acts across the lipid bilayer causes an effective far field tension, with σ the surface tension coefficient [53]. This means that remodeling the membrane away from a flat shape requires a surface energy ΔE_σ

$$\Delta E_\sigma = 2\pi \int_0^\infty \sigma R(1 - \cos\psi) dS. \tag{3}$$

ESCRT-proteins form a dynamic coat, *i.e.*, individual ESCRT-proteins are continuously recruited to and dissociate from the endosome membrane [20, 54]. The binding energy ΔE_μ between the membrane and the coat is proportional to the local ESCRT density ρ and the coat area

$$\Delta E_\mu = -2\pi \int_0^\infty \mu(\rho(S) - \rho_0) R dS, \tag{4}$$

with μ the binding energy per unit area. The second term in Eq. 4 subtracts the binding energy of a flat continuously coated membrane with a uniform ESCRT density ρ_0.

The amount of ESCRT proteins that can bind to the endosome membrane is limited, as they experience an effective steric repulsion [55, 56], primarily generated by volume exclusion, which we approximate up to second order in ρ by the second viral coefficient ν_2. The corresponding steric repulsion energy ΔE_s, is written as

$$\Delta E_\mathrm{s} = 2\pi \int_0^\infty \nu_2(\rho(S)^2 - \rho_o^2) R. \tag{5}$$

The second term in Eq. 5 subtracts the energy of a flat, uniformly coated membrane. Protein crowding has been shown theoretically and experimentally to be a mechanism that facilitates membrane deformation [56, 57]. Together, the binding energy (Eq. 4) and the steric repulsion (Eq. 5) represent the crowding effect that stem from the supercomplex of cargo proteins, ESCRT and clathrin.

The total change in energy ΔE as we start from a flat membrane and progress towards a budding membrane, is at each stage in the process given by the sum of the five energy contributions

$$\Delta E = \Delta E_\mathrm{g} + \Delta E_\kappa + \Delta E_\sigma + \Delta E_\mu + \Delta E_\mathrm{s}. \tag{6}$$

A non-uniform distribution of ESCRT proteins will lead to an additional energy term that penalizes large gradients in the density profile, which leads to an effective line tension at the boundary between the ESCRT-free and the coated region. However, this line tension contribution is a very small correction to the membrane energy (Supplementary information) and is neglected here. A spontaneous curvature induced by a protein-scaffold is not expected to play a significant role in ILV budding as $in-vitro$ experiments using GUVs have shown that ESCRTs do not coat ILVs [13]. In addition, a spontaneous curvature induced by cargo proteins can be disregarded as a cause for membrane shape remodeling, since ILVs serve as a sorting compartment for a large variety of transmembrane proteins and there is no biophysical indication that these proteins all induce the a simiar spontaneous curvature [58].

The ratio of the specific binding energy μ and the proportionality factor of the Gaussian bending rigidity γ_g defines an inverse length scale C_g that we use to express the membrane energy in dimensionless variables,

$$C_\mathrm{g} = \sqrt{\mu/\gamma_\mathrm{g}}. \tag{7}$$

We will show below that C_{g} corresponds to the mean curvature of the ESCRT-free ILV. The ratio of μ and the second virial coefficient ν_2 defines a density ρ_0, which is the baseline ESCRT density on the flat membrane $\rho_0 = \frac{\mu}{2\nu_2}$. Furthermore, we introduce the non-dimensional numbers $\widetilde{\sigma} = 2\sigma/(\mu\rho_0)$ and $\epsilon = \rho_0\gamma_{\mathrm{g}}/\kappa = \mu\gamma_{\mathrm{g}}/(2\nu_2\kappa)$, which dictate the energy landscape of the membrane remodeling process. $\widetilde{\sigma}$ describes the ratio between surface tension and binding energy, which increases for a high surface tension and for a small μ or a low ρ_0, *i.e.*, for a weak interaction between the ESCRT proteins and the endosome membrane or for a low ESCRT density on the non-deformed membrane. The tension σ in biological membranes can vary quite significantly $\sigma \cap 10^{-6} - 10^{-3}\mathrm{N/m}$ [59, 60, 61]. The interaction energy between biological membranes and proteins is typically in the range of $\mu \approx 1\mathrm{k_BT}$ [62]. The size of ESCRT proteins is in the order of 10nm [51, 63, 52], which in turn leads to an estimate for the ESCRT density of $\rho_0 \approx 0.01\ \mathrm{nm}^{-2}$. Combining these data gives us the expected physiological range of the dimensionless number $\widetilde{\sigma}$=0.01-10. ϵ describes the ratio of bending rigidities associated with the mean and the Gaussian curvature, which are typically in the same order of magnitude [64] and we expect $\epsilon = \mathcal{O}(1)$.

ESCRT density on the endosome: The ESCRT proteins form a stable microdomain at the endosome for several minutes. However, individual ESCRT-proteins are rapidly exchanged within a few seconds [54, 20], which suggests that the ESCRTs can quickly adopt their local density to changes in the membrane curvature in order to minimize the overall energy. By minimizing Eq. 6 with respect to the ESCRT density ρ gives us a relation between ρ and the principal curvatures

$$\rho = \rho_0 \left[1 - \frac{C_1 C_2}{C_{\mathrm{g}}^2}\right]. \tag{8}$$

We see from Eq. 8 that the ESCRT density is uniform with $\rho = \rho_0$ when $C_1 = 0$ or $C_2 = 0$, *i.e.*, on a flat membrane. In contrast, the protein density is reduced where the membrane exhibits a positive Gaussian curvature, *i.e.*, at the center of the budding vesicle, while ρ increases in regions of negative Gaussian curvature, *i.e.*, in the neck region of the vesicle. Eq. 8 reveals that an ESCRT-free membrane bud, with $\rho = 0$, follows from a spherical membrane shape, where both principal curvatures are given by $C_1 = C_2 = C_{\mathrm{g}}$. The curvature C_{g} of the ESCRT-free region (Eq. 7) is determined by a balance between binding energy and the Gaussian bending rigidity. To gain a deeper understanding of the parameters that determine the vesicle curvature, we consider the individual contributions to the membrane energy Eq. 2-6. There are two terms that can generate a negative contribution to the energy: the binding energy ΔE_μ and the Gaussian bending energy ΔE_{g}. For a uniform ESCRT coat the Gaussian bending rigidity is constant along the membrane, which means that ΔE_{g} becomes zero according to the Gauss-Bonnet theorem [65]. In contrast, if a coat-free membrane bud forms, the system gains energy in the form of a Gaussian bending energy but pays an energetic penalty due to a reduced binding energy. It is the balance between binding energy and Gaussian bending rigidity that determines the curvature of the ESCRT-free ILV.

Endosome membrane shapes and ESCRT density profiles: The membrane shape and energy depend only on the curvature C_{g} and the dimensionless numbers ϵ and $\widetilde{\sigma}$. In Fig. 1c and [15] we determine an average ILV diameter of 46nm, which is equivalent to a curvature $C_{\mathrm{g}} \approx 0.04\ \mathrm{nm}^{-1}$. Defining the curvature C_{g} from experimental measurements enables a reduction of the number of free parameters in our model to just two, ϵ and $\widetilde{\sigma}$.

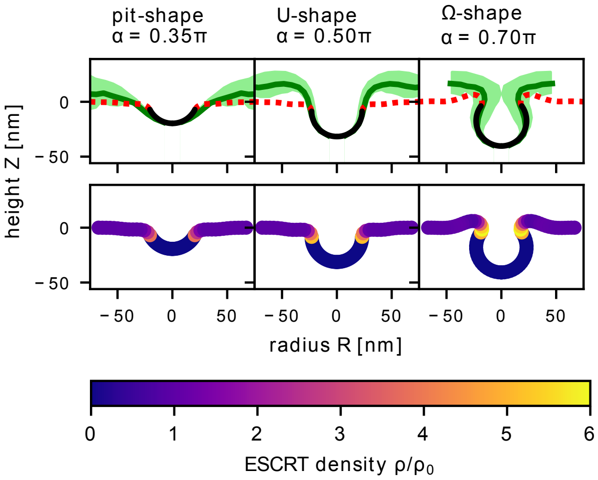

Figure 3: Vesicle budding: We compare the experimentally obtained endosome shapes with the minimal energy shapes (Eq. 6) for different angles α, when $\epsilon = 2$ and $\widetilde{\sigma} = 0.1$. (top row) Experimental membrane shapes are grouped into three categories: pit-shape ($\alpha = 0.35\pi$), U-shape ($\alpha = 0.5\pi$) and Ω-shape ($\alpha = 0.7\pi$). For each subgroup the average shape is shown as a solid green line, while the standard deviation is indicated by the shaded area. The ESCRT-free vesicle bud is shown by the solid black line, while the coated region is shown by the red dashed line. (bottom row) The ESCRT density is shown along the membrane for the three characteristic shapes, which exhibits an elevated ESCRT density in the neck region.

If the membrane adopts a spherical shape with a mean curvature C_g, the ESCRT-free area is given by $A_\mathrm{f} = 2\pi/C_\mathrm{g}^2(1 - \cos\alpha)$, with α the angle formed between the tip of the bud at the Z-axes and the start of the ESCRT coated region as illustrated in Fig. 2. To understand how the membrane energy changes as this region increases, we minimize the total energy Eq. 6 under the constraint that α is fixed. We have fixed ϵ=2.0 and $\widetilde{\sigma}$=0.1, which leads to an energy barrier that is similar to our analytical estimate based on the characteristic ESCRT-recruitment time scales, ΔE_B ≈0.6k$_\mathrm{B}$T. Fig. 3 shows the quasi-static membrane shape predicted by our mathematical model and the ESCRT density together with the experimental membrane shapes. The experimental ILV shapes are illustrated by the solid lines, while the standard deviation is indicated by a shaded area, obtained from ten budding profiles each [15]. From the comparison between the mathematical model and the experimental data we determine the opening angle α=0.35π, 0.5π, 0.7π, corresponding to pit-shape, U-shape and Ω-shape.

We turn next to see if the model can also help to understand the $in-vitro$ experimental observations based on GUVs, which have also demonstrated ESCRT-mediated membrane budding in the absence of ESCRT-III. The size of the vesicles formed in these experiments, with a typical vesicle diameter in the μm range, differs largely from ILVs [13]. According to Eq. 7 the size difference stems from a variation of the specific binding energy μ or the Gaussian bending rigidity, quantified by the proportionality factor γ_g. We expect that the capability of ESCRT proteins to induce a Gaussian bending rigidity to be similar in both the *in-vivo* and *in-vitro* system, giving nearly the same γ_g. The variation in vesicle size is therefore attributed to different values of the specific binding energy μ, which we suspect is lower in GUV experiments as they lack cargo proteins. A significant increase of the ESCRT density was found in the vesicle neck region on GUVs [13], which is also predicted by our theoretical model (Fig. 3). We observe that when the membrane has an Ω- shape, the ESCRT density profile has a pronounced maximum in the neck region that is six times greater than ρ_0.

ESCRT-mediated membrane deformation does not require energy: In Fig. 4a) we show how the membrane energy depends on α as we go from a flat membrane ($\alpha = 0$) to an Ω-shaped membrane ($\alpha/\pi \to 1$) for three different combinations of ϵ and $\widetilde{\sigma}$, where ϵ=2.0 and $\widetilde{\sigma}$=0.1 correspond to physiologically realistic values, while ϵ=1.3, $\widetilde{\sigma}$=0.5 andϵ=0.6 and $\widetilde{\sigma}$=0.9 result in an energy barrier that cannot be overcome by thermal fluctuations and thus prevents ILV formation.

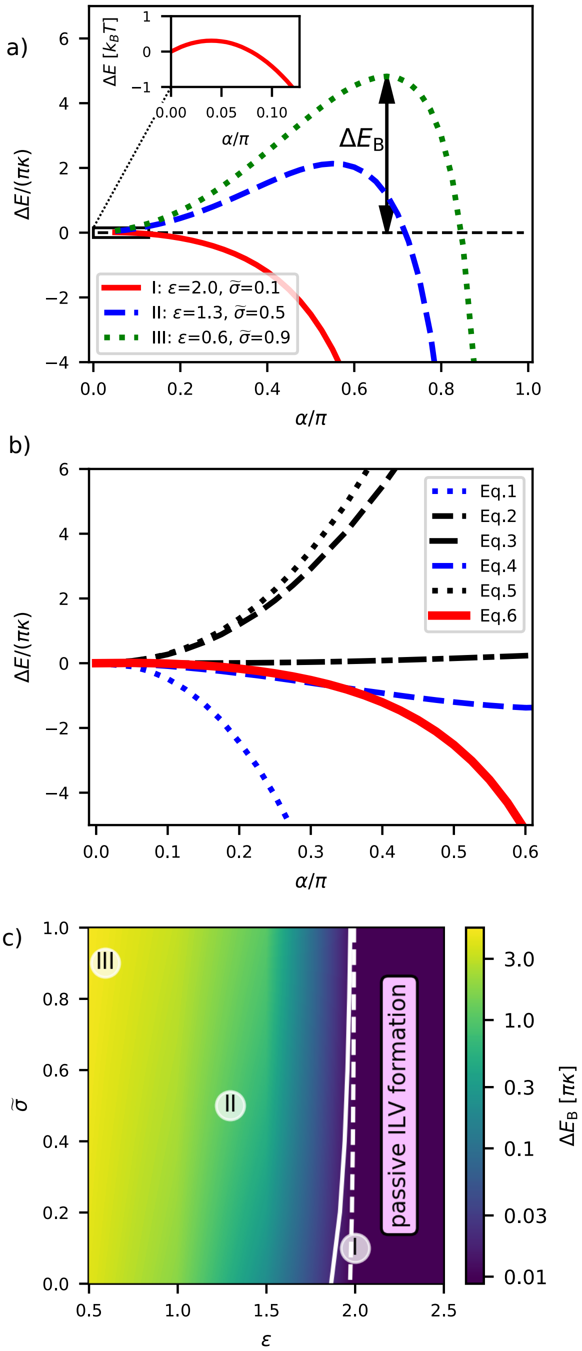

Figure 4: Energy barrier: a) To understand how the energy changes with the shape changes of the membrane, we plot ΔE_{B} as a function of the opening angle α for (I) ϵ =2.0, $\widetilde{\sigma}$=0.1; (II) ϵ =1.3, $\widetilde{\sigma}$=0.5 and (III) ϵ =0.6, $\widetilde{\sigma}$=0.9. The energy landscape (I), solid red line, corresponds to the membrane shape transition shown in Fig. 3. Inset: The maximum of the energy for ϵ =2.0, $\widetilde{\sigma}$=0.1 is found around α/π=0.04. To convert the energy into units of $\mathrm{k_B T}$, the bending rigidity is set to κ=10$\mathrm{k_B T}$ [23]. b) We plot the different contributions of ΔE_{b} (Eq. 1-5) together with the total energy Eq. 6 for (I) ϵ=2.0, $\widetilde{\sigma}$=0.1 to help illustrate which part produces a positive (inhibiting ILV formation) and negative (promoting ILV formation) energy. It is clear that both steric repulsion of proteins and bending of the membrane is energetically costly, while the Gaussian bending energy becomes negative and grows in magnitude as ILV formation takes place ($\alpha/\pi \to 1$). c) We scan the phase space in ϵ (ratio of the bending rigidities associated with the mean and the Gaussian curvature) and $\widetilde{\sigma}$ (ratio of surface tension and binding energy) in numerical simulations to determine their influence on the energy barrier ΔE_{B}. The magnitude of the energy barrier is shown as a color map with a logarithmic scale. The threshold energy barrier for passive ILV formation is illustrated by the solid line when ΔE_{B}=2.0$\mathrm{k_B T}$ and the analytical estimate for the energy barrier of ILV formation, ΔE_{B}=0.6$\mathrm{k_B T}$ is shown by a dashed line.

To better understand which part of the energy contributions dominates during the shape transition we show the individual contributions to the energy together with the total membrane energy for ϵ=2.0, $\widetilde{\sigma}$=0.1 in Fig. 4b). The change in both binding energy (Eq. 4) and surface tension (Eq. 3) are small compared to the overall change in energy. The energy generated by the steric repulsion of proteins (Eq. 5) and the bending of the membrane (Eq. 2) both increase continuously, thus opposing ILV formation. The only sizeable negative contribution comes from the Gaussian bending term (Eq. 1), which dominates the total membrane energy as the membrane shape approaches scission ($\alpha/\pi \to 1$). The divergence of the Gaussian energy as the angle approaches $\alpha/\pi \to 1$ is a characteristic of the large local variation of the Gaussian bending rigidity. Theoretical studies have shown that a partially formed vesicle and a finite vesicle neck is not stable, *i.e.*, the energy diverges, if the variation in Gaussian bending rigidity is large compared to the bending rigidity associated with mean curvature [66].

Next, we scan the phase space of $\epsilon \in [0.5-2.5]$ and $\widetilde{\sigma} \in [0-1]$ in numerical simulations, where we minimize the energy (Eq. 6) to determine the magnitude of the energy barrier ΔE_{B} as a function of α. In Fig. 4c), we see that ΔE_{B} decreases with increasing ϵ and decreasing $\widetilde{\sigma}$. In Fig. 4c) we illustrate the region where an ILV is formed passively, by drawing a solid line for ΔE_{B}=2k$_{\mathrm{B}}$T, which for a bending rigidity of κ=10k$_{\mathrm{B}}$T [23] is equivalent to $\Delta E_{\mathrm{B}}/(\pi\kappa) \approx$0.06 in dimensionless units. In addition, we show a dashed line for ΔE_{B}=0.6k$_{\mathrm{B}}$T as determined by our analyzes as an estimate for the energy barrier of ILV formation. The phase space in Fig. 4c) shows that passive ILV formation is feasible for a wide range of values for $\widetilde{\sigma}$ and ϵ. **Neck closure:** $In-vitro$ experiments on GUVs have shown that ESCRT-III and Vsp4 alone are sufficient to induce vesicle formation with an inverse topology, similar to $in-vivo$ ILV budding [67]. However, in ILV formation both early ESCRTs (ESCRT-0, -I, -II) and ESCRT-III as well as Vsp4 and cargo proteins are present, which play different and crucial roles in cargo sorting and ILV formation. The mathematical description of the ILV formation puts us in the position to relate the ESCRT recruitment dynamics with the transient membrane shapes. We determine the amount of excess ESCRT proteins (Δn) as the integral over the protein density on the membrane, where the ESCRT density exceeds the baseline value ρ_0. In rescaled units Δn reads as

$$\Delta n = \int_{s^*}^{\infty} r\left(1-\frac{\rho}{\rho_0}\right) ds = \int_{s^*}^{\infty} \frac{d\phi}{ds}\sin\phi = 1-\cos\alpha, \tag{9}$$

with s^* the arc length where the ESCRT coated region begins. While the membrane under goes a shape transition from a flat surface to an Ω-shape, Δn appears to increase continuously. The experimental measurement of the fluorescent signal of ESCRT-0 is proportional to Δn. Hence, Eq. 9 enables us to determine the shape evolution in terms of the time dependency of α from the fluorescent ESCRT-0 signal (Methods section). The corresponding time evolution of α, shown in Fig. 5b, reveals a continuous rather than a jump-like vesicle formation in accordance with the experimental observations (Fig. 5a and [15]).

ESCRT-III mediated scission of the membrane neck is the final step of ILV formation and ESCRT-III exhibits a preferred binding to curved regions of the membrane [27]. To quantify the membrane curvature in the ILV neck, we define the magnitude of the rescaled Gaussian curvature as $K_{\mathrm{g}} := \left(\frac{C_1 C_2}{C_{\mathrm{g}}^2}\right)_{\mathrm{neck}}$ at the boundary between ESCRT-free and - coated region. Fig. 5c shows K_{g} for six combinations of $\widetilde{\sigma}$ and ϵ, with $\epsilon \in [2.0, 2.5]$ and $\widetilde{\sigma} \in [0.0, 1.0]$, *i.e*, in the regime of passive ILV formation, where we see that all data points collapse on to a single curve exhibiting the same behavior. It illustrates that even though the energy barrier strongly depends on ϵ, the Gaussian curvature is a key feature of the membrane shape depending only marginally on the parameters $\widetilde{\sigma}$ and ϵ, *i.e.*, the membrane shape is robust towards fluctuations in membrane tension and bending rigidity. By comparing the fluorescent signal of ESCRT-III and the Gaussian curvature in the neck region, we speculate that the steep decrease of the Gaussian curvature K_{g}, tiggers the assembly of ESCRT-III and subsequently leads to membrane scission forming an ILV.

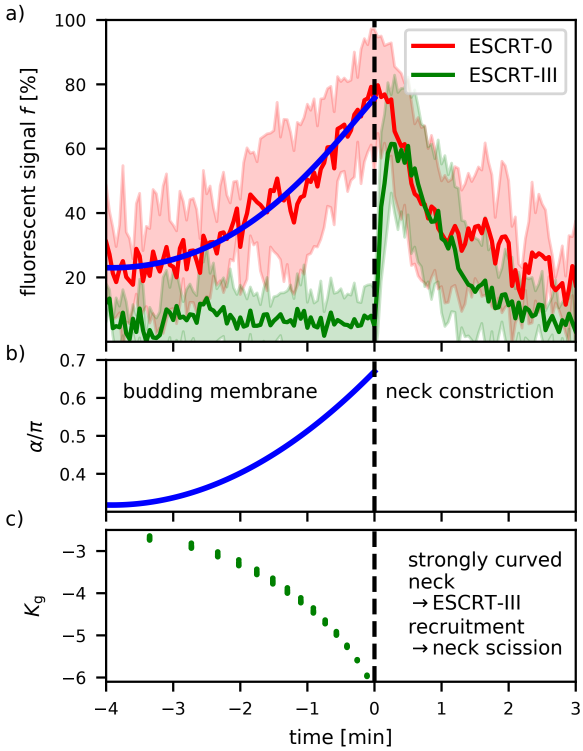

Figure 5: ESCRT-III recruitment: a) The experimental signal intensity of fluorescently labeled HRS (ESCRT-0) and CHMP4B (ESCRT-III) is shown as a function of time. The average over 23 isolated signal curves is shown together with the standard deviation (shaded area). The fluorescent signal of ESCRT-0 is proportional to the amount of adsorbed proteins, which allows us correlate the magnitude of the fluorescent signal with the opening angle α (Methods Section). Figure reproduced from [15] b) By combining the experimentally measured time evolution of the fluorescent marker with the theoretically predicted membrane shapes, we determine the time evolution of α according to the fit in subfigure a. c) The Gaussian curvature in the neck, *i.e.*, at the boundary between ESCRT-free and - coated region, is determined for six different combinations of ϵ, $\widetilde{\sigma}$, with $\epsilon \in [2.0, 2.5]$ and $\widetilde{\sigma} \in [0.0, 1.0]$. The Gaussian curvature strongly increases in magnitude as the membrane transitions from a flat to an Ω-shape.

Discussion

By combining mathematical modeling and cell biological data we are able to point to the biophysical determinants that facilitate ILV budding by early ESCRTs, which is a consequence of the interplay between ESCRT-induced Gaussian bending rigidity and their crowding on the membrane. Our mathematical model highlights that while ESCRT dissociation at the budding site is biologically desirable, since it enables the cell to reuse the ESCRT proteins, it is also a physical prerequisite to form an ILV as the systems benefits from the negative energy from Gaussian bending only if the Gaussian bending rigidity, or equivalently the ESCRT-density, is non-homogenously distributed at the membrane. The ILV size is set by a balance between the loss of binding energy in the ESCRT-free region and by the increase of the Gaussian bending energy in the neck region. Our model predicts; (i) a high density of ESCRTs in the membrane neck, (ii) the shape of the endosome membrane during budding (pit-, U- and Ω- shape), (iii) vesicle formation to be a continuous process in time, all in accordance with experimental observations.

By treating the experimental time scales for recruitment of ESCRTs as a diffusive process we analytically predict the energy barrier the system must overcome to form a vesicle $\Delta E_{\mathrm{B}} \approx 0.6 \mathrm{k_B T}$. Furthermore, our mathematical model that accounts for membrane bending, binding and crowding of proteins, and the spatial distribution of the early ESCRTs, shows that membrane budding is a self-organized passive process, that does not need ATP consumption, which explains, why it is sufficient for the ATPase Vps4 to bind to the ESCRT complex in the final stage of membrane constriction and scission [19]. By scanning the phase space in the ratio of bending rigidities (ϵ) and the ratio of the surface tension and the binding energy ($\widetilde{\sigma}$) in numerical simulations, we show that ILVs may form passively over a wide range of parameters. Thus, to inhibit membrane budding the system must be perturbed such that the energy barrier exceeds beyond the range that can be affected by thermal fluctuations. We predict that a change in membrane tension by a hypertonic shock (changing $\widetilde{\sigma}$), would suppress ILV formation. The energy landscape is also sensitive to changes of the bending rigidities (changing ϵ), which leads us to speculate about the role of the clathrin layer that is bound to the ESCRT microdomain. The physical properties of the clathrin layer are not yet understood. We have shown earlier that ILV formation is severely impaired in the absence of clathrin recruitment to endosomes [15], which we can now rationalize in the framework of our model, where absence of clathrin binding corresponds to an effective decrease the binding energy μ (*i.e.* ϵ is reduced) and stalls ILV formation through a higher energy barrier.

We used the predicted ESCRT density from the quasi-static theoretical model to correlate it to the increase in the fluorescent intensity of ESCRT-0, which gives a prediction of the opening angle α over time. Our analysis point to a continuous rather than jump-like transition from a pit-shape, to a U-shape and an Ω-shape, in concordance with the fact that there are no overweight in samples for either of these shape categories found in the TEM images of different endosomes and at random time points in the budding process. Together this leads us to argue that early ESCRTs play a crucial role not only in sequestering cargo proteins, but also in the membrane shape remodeling in accordance with earlier work on GUVs [13]. Importantly, our data points to the early ESCRTs as determinants for the initial membrane budding: Fluorescence microscopy data shows that ESCRT-0 and ESCRT-I get enriched at the endosome membrane over several minutes. On a flat membrane this would lead to a significant increase in steric repulsion between the ESCRT proteins and an energy increase. Instead, the system evades an energetic penalty by forming a membrane bud in the pathway to ILV formation.

The membrane shape transition is accompanied by a steep decline in the Gaussian curvature in the neck region, which we believe is a trigger for ESCRT-III assembly to facilitate membrane scission, since ESCRT-III binds preferentially to negatively curved membranes [27]. Qualitatively similar ESCRT-III recruitment dynamics have been found in HIV budding [68], where Gag proteins assemble on the membrane over a longer time span, while ESCRT-III shows a spike-like recruitment over time. HIV budding, where the Gag proteins cause an effective spontaneous curvature [69, 68], resembles ESCRT-induced ILV budding morphologically. In particular, the formation of a curved membrane neck, is likely a prerequisite in both cases to promote ESCRT-III assembly [27].

Together these observations show that the experimentally measured increase in the fluorescent signal of early ESCRTs is a hallmark of the change in membrane shape at the endosome. This implicates the early ESCRTs together with clathrin and cargo proteins in the membrane remodeling process and adding to their role as cargo sorting molecules. The generic nature of protein crowding and a spatially varying Gaussian bending rigidity on cell membranes suggest that the developed model can have implications beyond understanding budding of ILVs by early ESCRTs, as it may also help understand other membrane remodeling processes.

Methods

Electron microscopy and measurements: HeLa cells were grown on poly-l-lysine coated sapphire discs. To label newly internalized EGFR following EGF-stimulation, cells were first washed with ice cold PBS and incubated on ice with an antibody recognizing the extracellular part of EGFR (mouse anti-EGFR, Pharmingen). After washing four times with ice cold PBS, cells were incubated with Protein A-10 nm gold conjugate (UMC Utrecht Dept. of Cell Biology) which recognizes the Fc portion of the mouse IgG2b primary antibody. Cells were again washed four times with ice cold PBS and then stimulated with EGF in warm DMEM for indicated amounts of time before high pressure freezing was done. Sapphire discs were high pressure frozen using a Leica HPM100, and freeze substitution was performed as follows: sample carriers designed for sapphire discs were filled with 4 ml of freeze substituent (0.1% (w v-1) uranyl acetate in acetone, 1% H_2O) and placed in a temperature-controlling AFS2 (Leica) equipped with an FPS robot. Freeze-substitution occurred at -90^{o}C for 48 h before the temperature was raised to -45^{o}C over a time span of 9 h. The samples were kept in the freeze substituent at -45^{o}C for 5 hours before washing 3 times with acetone followed by a temperature increase (5^{o}C per hour) to -35^{o}C, and then infiltrated with increasing concentrations of Lowicryl HM20 (10%, 25%, 75%, 4h each). During the last two steps, temperature was gradually raised to -25^{o}C before infiltrating 3 times with 100% Lowicryl (10 h each). Subsequent UV-polymerization was initiated for 48 h at -25^{o}C, and the temperature was then evenly raised to +20^{o}C (5^{o}C per hour). Polymerization then continued for another 24 h at 20^{o}C. Serial sections ($\sim$150 nm for counting ILVs in endosomes; 150-250 nm for tomography) were cut on an Ultracut UCT ultramicrotome (Leica, Germany) and collected on formvar coated mesh grids. Samples were observed at 80 kV in a JEOL-JEM 1230 electron microscope and images were recorded using iTEM software with a Morada camera (Olympus, Germany). Samples that were prepared for tomography were observed in a Thermo ScientificTM TalosTM F200C microscope and image series were taken between -60^o and 60^o tilt angles with 2^o increment. Single-tilt axes series were recorded with a Ceta 16M camera. Tomograms were computed using weighted back projection using the IMOD package. Display and segmentation of tomograms were also performed using IMOD software version 4.9 70. Measurements of endosome and ILV diameters were done in FIJI with the measurement tool.

Energy minimization: We rescale all lengths with C_g giving the dimensionless variables: $s = C_g \cdot S$, $r = C_g \cdot R$, $\psi(S) \to \phi(s)$. By introducing this scaling of the variables we rewrite Eq. 6 in dimensionless form as

$$\frac{\Delta E}{\pi\kappa} = \int_0^\infty \left[r\left(\frac{d\phi}{ds}+\frac{\sin\phi}{r}\right)^2 + \epsilon r\left(\frac{\rho}{\rho_0}-1\right)^2 + 2\epsilon\frac{\rho}{\rho_0}\frac{d\phi}{ds}\sin\phi + \widetilde{\sigma}\epsilon r(1-\cos\phi)\right] ds. \tag{10}$$

For any angle α the membrane shape in the inner region is described by a spherical cap with rescales mean curvature 1. The shape as well as the energy contribution in rescaled units are hence obtained analytically as $r = \sin\phi$, $z = 1-\cos\phi$ and $E_{\text{inner}} = \pi\kappa(1-\cos\alpha)\left[4+(\widetilde{\sigma}+1)\epsilon\right] - \widetilde{\sigma}\epsilon/2\sin^2\alpha$. To minimize the total energy in the outer region numerically, we define a total arc length s_{end} at which the angle ϕ reaches zero. We set $s_{\text{end}} = 15$ to approximate the limit of an infinitely large surface. Similar to the method described by Rozycki et al. [39] we describe the angle ϕ in the outer region as a truncated Fourier series:

$$\phi(s) = \alpha\left(1-\frac{s}{s_{\text{end}}}\right) + \sum_{i=1}^{25}\phi_i \sin\left(i\pi\frac{s}{s_{\text{end}}}\right) \tag{11}$$

The radius r is then obtained from the relation $dr/ds = \cos\phi$. The prefactors ϕ_i are obtained by minimizing the energy Eq. 10 using the python *basinhopping* routine [70] (Supplementary information).

Fluorescent signal fit: The intensity of the experimentally measured fluorescent signal f is assumed to be proportional to Δn. To relate both quantities, we recall that the membrane shapes, which are closest to a fully formed ILV are Ω-shaped with an angle α=0.7π. We therefore assume the maximum of the fluorescent signal to correspond to $\Delta n^* = \Delta n(\alpha = 0.7\pi) = 1.59$, which allows to predict how α varies in time in the experiment by fitting the fluorescent signal (Fig. 5a) to

$$f(t) = \frac{1-\cos\alpha(t)}{\Delta n*}, \text{with } \alpha(t) = \pi\left[\alpha_0 + \left(\frac{t-t_0}{\tau}\right)^2\right], \tag{12}$$

with the fit parameters α_0=0.32, t_0=-3.9min, τ=6.6min, where τ describes the characteristic time over which the fluorescent signal increases and α_0 together with t_0 account for an offset due to the background noise of the fluorescent signal.

References

[1] M. Sachse, S. Urbe, V. Oorschot, G. J. Strous, and J. Klumperman, “Bilayered clathrin coats on endosomal vacuoles are involved in protein sorting toward lysosomes,” *Mol. Biol. Cell*, 13, 4, 1313–1328, **2002**.

[2] S. D. Conner and S. L. Schmid, “Regulated portals of entry into the cell,” *Nature*, 422, 6927, 37–44, **2003**.

[3] A. Sorkin and M. von Zastrow, “Endocytosis and signalling: intertwining molecular networks,” *Nat. Rev. Mol. Cell Biol.*, 10, 9, 609–622, **2009**.

[4] C. Raiborg, T. E. Rusten, and H. Stenmark, “Protein sorting into multivesicular endosomes,” *Curr. Opin. Cell Biol.*, 15, 4, 446–455, **2003**.

[5] C. Raiborg and H. Stenmark, “The ESCRT machinery in endosomal sorting of ubiquitylated membrane proteins,” *Nature*, 458, 7237, 445–452, **2009**.

[6] C. Mattissek and D. Teis, “The role of the endosomal sorting complexes required for transport (ESCRT) in tumorigenesis,” *Mol. Membr. Biol.*, 31, 4, 111–119, **2014**.

[7] M. Colombo, G. Raposo, and C. Thery, “Biogenesis, Secretion, and Intercellular Interactions of Exosomes and Other Extracellular Vesicles,” *Annu. Rev. Cell Dev. Biol., Vol 30*, **2014**.

[8] L. Belov, K. J. Matic, S. Hallal, O. G. Best, S. P. Mulligan, and R. I. Christopherson, “Extensive surface protein profiles of extracellular vesicles from cancer cells may provide diagnostic signatures from blood samples,” *J. Extracell. Vesicles*, 5, p. UNSP 25355, **2016**.

[9] L. Milane, A. Singh, G. Mattheolabakis, M. Suresh, and M. M. Amiji, "Exosome mediated communication within the tumor microenvironment," *J. Controlled Release*, 219, 278–294, **2015**.

[10] J. H. Hurley, "ESCRTs are everywhere," *EMBO J*, 34, 19, 2398–2407, **2015**.

[11] F. R. Maxfield and T. E. McGraw, "Endocytic recycling," *Nat. Rev. Mol. Cell Biol.*, 5, 2, 121–132, **2004**.

[12] C. M. Fader and M. I. Colombo, "Autophagy and multivesicular bodies: two closely related partners," *Cell Death Differ.*, 16, 1, 70–78, **2009**.

[13] T. Wollert and J. H. Hurley, "Molecular mechanism of multivesicular body biogenesis by ESCRT complexes," *Nature*, 464, 7290, 864–U73, **2010**.

[14] W. M. Henne, N. J. Buchkovich, and S. D. Emr, "The ESCRT Pathway," *Dev. Cell*, 21, 1, 77–91, **2011**.

[15] E. M. Wenzel, S. W. Schultz, K. O. Schink, N. M. Pedersen, V. Nahse, A. Carlson, A. Brech, H. Stenmark, and C. Raiborg, "Concerted ESCRT and clathrin recruitment waves define the timing and morphology of intraluminal vesicle formation," *Nat. Commun.*, 9, p. 2932, **2018**.

[16] G. Raposo, D. Tenza, D. M. Murphy, J. F. Berson, and M. S. Marks, "Distinct protein sorting and localization to premelanosomes, melanosomes, and lysosomes in pigmented melanocytic cells," *J. Cell Biol.*, 152, 4, 809–823, **2001**.

[17] C. Raiborg, K. G. Bache, A. Mehlum, E. Stang, and H. Stenmark, "Hrs recruits clathrin to early endosomes," *EMBO J*, 20, 17, 5008–5021, **2001**.

[18] C. Raiborg, K. G. Bache, D. J. Gillooly, I. H. Madshush, E. Stang, and H. Stenmark, "Hrs sorts ubiquitinated proteins into clathrin-coated microdomains of early endosomes," *Nat. Cell Biol.*, 4, 5, 394–398, **May 2002**.

[19] M. A. Y. Adell, G. F. Vogel, M. Pakdel, M. Muller, H. Lindner, M. W. Hess, and D. Teis, "Coordinated binding of Vps4 to ESCRT-III drives membrane neck constriction during MVB vesicle formation," *J. Cell Biol.*, 205, 1, 33–49, **2014**.

[20] M. A. Y. Adell, S. M. Migliano, S. Upadhyayula, Y. S. Bykov, S. Sprenger, M. Pakdel, G. F. Vogel, G. Jih, W. Skillern, R. Behrouzi, M. Babst, O. Schmidt, M. W. Hess, J. A. G. Briggs, T. Kirchhausen, and D. Teis, "Recruitment dynamics of ESCRT-III and Vps4 to endosomes and implications for reverse membrane budding," *Elife*, 6, p. e31652, **2017**.

[21] J. Schoneberg, M. R. Pavlin, S. Yan, M. Righini, I. H. Lee, L. A. Carlson, A. H. Bahrami, D. H. Goldman, X. F. Ren, G. Hummer, C. Bustamante, and J. H. Hurley, "ATP-dependent force generation and membrane scission by ESCRT-III and Vps4," *Science*, 362, 6421, p. 1423, **2018**.

[22] W. Helfrich, "Elastic Properties of Lipid Bilayers - Theory and Possible Experiments," *Z. Naturforsch. C*, C 28, 11-1, 693–703, **1973**.

[23] R. Dimova, "Recent developments in the field of bending rigidity measurements on membranes," *Adv. Colloid Interface Sci.*, 208, 225–234, **2014**.

[24] K. B. Quinney, E. B. Frankel, R. Shankar, W. Kasberg, P. Luong, and A. Audhya, "Growth factor stimulation promotes multivesicular endosome biogenesis by prolonging recruitment of the late-acting ESCRT machinery," *Proc. Natl. Acad. Sci. USA*, **2019**.

[25] N. Chiaruttini, L. Redondo-Morata, A. Colom, F. Humbert, M. Lenz, S. Scheuring, and A. Roux, "Relaxation of Loaded ESCRT-III Spiral Springs Drives Membrane Deformation," *Cell*, 163, 4, 866–879, **2015**.

[26] H. G. Franquelim and P. Schwille, "Revolving around constriction by ESCRT-III," *Nat. Cell Biol.*, 19, 7, 754–756, **2017**.

[27] I. H. Lee, H. Kai, L. A. Carlson, J. T. Groves, and J. H. Hurley, "Negative membrane curvature catalyzes nucleation of endosomal sorting complex required for transport (ESCRT)-III assembly," *Proc Natl Acad Sci U S A*, 112, 52, 15 892–15 897, **2015**.

[28] N. Elia, G. Fabrikant, M. M. Kozlov, and J. Lippincott-Schwartz, "Computational Model of Cytokinetic Abscission Driven by ESCRT-III Polymerization and Remodeling," *Biophys. J.*, 102, 10, 2309–2320, **2012**.

[29] I. Goliand, S. Adar-Levor, I. Segal, D. Nachmias, T. Dadosh, M. M. Kozlov, and N. Elia, "Resolving ESCRT-III Spirals at the Intercellular Bridge of Dividing Cells Using 3D STORM," *Cell Rep.*, 24, 7, 1756–1764, **2018**.

[30] N. Elia, R. Sougrat, T. A. Spurlin, J. H. Hurley, and J. Lippincott-Schwartz, "Dynamics of endosomal sorting complex required for transport (ESCRT) machinery during cytokinesis and its role in abscission," *Proc Natl Acad Sci U S A*, 108, 12, 4846–4851, **2011**.

[31] M. Bleck, M. S. Itano, D. S. Johnson, V. K. Thomas, A. J. North, P. D. Bieniasz, and S. M. Simon, "Temporal and spatial organization of ESCRT protein recruitment during HIV-1 budding," *Proc Natl Acad Sci U S A*, 111, 33, 12 211–12 216, **2014**.

[32] N. De Franceschi, M. Alqabandi, N. Miguet, C. Caillat, S. Mangenot, W. Weissenhorn, and P. Bassereau, "The ESCRT protein CHMP2B acts as a diffusion barrier on reconstituted membrane necks," *J. Cell Sci.*, 132, 4, p. 217968, **2019**.

[33] J. Arii, M. Watanabe, F. Maeda, N. Tokai-Nishizumi, T. Chihara, M. Miura, Y. Maruzuru, N. Koyanagi, A. Kato, and Y. Kawaguchi, "ESCRT-III mediates budding across the inner nuclear membrane and regulates its integrity," *Nat. Commun.*, 9, p. 3379, **2018**.

[34] M. L. Dustin and J. A. Cooper, “The immunological synapse and the actin cytoskeleton: molecular hardware for T cell signaling,” *Nat. Immunol.*, 1, 1, 23–29, **Jul. 2000**.

[35] M. Lenz, D. J. G. Crow, and J. F. Joanny, “Membrane Buckling Induced by Curved Filaments,” *Phys. Rev. Lett.*, 103, 3, p. 038101, **Jul. 2009**.

[36] M. M. Kozlov, H. T. McMahon, and L. V. Chernomordik, “Protein-driven membrane stresses in fusion and fission,” *Trends Biochem. Sci.*, 35, 12, 699–706, **Dec. 2010**.

[37] J. Agudo-Canalejo and R. Lipowsky, “Domes and cones: Adhesion-induced fission of membranes by ESCRT proteins,” *PLoS Comput Biol*, 14, 8, p. e1006422, **2018**.

[38] E. Boura, B. Rozycki, H. S. Chung, D. Z. Herrick, B. Canagarajah, D. S. Cafiso, W. A. Eaton, G. Hummer, and J. H. Hurley, “Solution Structure of the ESCRT-I and -II Supercomplex: Implications for Membrane Budding and Scission,” *Structure*, 20, 5, 874–886, **2012**.

[39] B. Rozycki, E. Boura, J. H. Hurley, and G. Hummer, “Membrane-Elasticity Model of Coatless Vesicle Budding Induced by ESCRT Complexes,” *PLoS Comput Biol*, 8, 10, p. e1002736, **2012**.

[40] M. Mercker and A. Marciniak-Czochra, “Bud-Neck Scaffolding as a Possible Driving Force in ESCRT-Induced Membrane Budding,” *Biophys. J.*, 108, 4, 833–843, **2015**.

[41] J. Liu, Y. D. Sun, D. G. Drubin, and G. F. Oster, “The Mechanochemistry of Endocytosis,” *PLoS Biol*, 7, 9, p. e1000204, **2009**.

[42] N. Cordella, T. J. Lampo, S. Mehraeen, and A. J. Spakowitz, “Membrane Fluctuations Destabilize Clathrin Protein Lattice Order,” *Biophys. J.*, 106, 7, 1476–1488, **Apr. 2014**.

[43] J. Liu, M. Kaksonen, D. G. Drubin, and G. Oster, “Endocytic vesicle scission by lipid phase boundary forces,” *Proc Natl Acad Sci U S A*, 103, 27, 10 277–10 282, **Jul. 2006**.

[44] J. Liu, Y. D. Sun, G. F. Oster, and D. G. Drubin, “Mechanochemical crosstalk during endocytic vesicle formation,” *Curr. Opin. Cell Biol.*, 22, 1, 36–43, **Feb. 2010**.

[45] S. Dmitrieff and F. Nedelec, “Membrane Mechanics of Endocytosis in Cells with Turgor,” *PLoS Comput Biol*, 11, 10, p. e1004538, **Oct. 2015**.

[46] K. Manakova, H. M. Yan, J. Lowengrub, and J. Allard, “Cell Surface Mechanochemistry and the Determinants of Bleb Formation, Healing, and Travel Velocity,” *Biophys. J.*, 110, 7, 1636–1647, **Apr. 2016**.

[47] W. K. Kim and R. R. Netz, “The mean shape of transition and first-passage paths,” *J. Chem. Phys.*, 143, 22, p. 224108, **2015**.

[48] A. R. Braun, E. Sevcsik, P. Chin, E. Rhoades, S. Tristram-Nagle, and J. N. Sachs, “alpha-Synuclein Induces Both Positive Mean Curvature and Negative Gaussian Curvature in Membranes,” *J. Am. Chem. Soc.*, 134, 5, 2613–2620, **2012**.

[49] Y. X. Mao, A. Nickitenko, X. Q. Duan, T. E. Lloyd, M. N. Wu, H. Bellen, and F. A. Quiocho, “Crystal structure of the VHS and FYVE tandem domains of Hrs, a protein involved in membrane trafficking and signal transduction,” *Cell*, 100, 4, 447–456, **2000**.

[50] M. S. Kostelansky, C. Schluter, Y. Y. C. Tam, S. Lee, R. Ghirlando, B. Beach, E. Conibear, and J. H. Hurley, “Molecular architecture and functional model of the complete yeast ESCRT-I heterotetramer,” *Cell*, 129, 3, 485–498, **2007**.

[51] X. F. Ren, D. P. Kloer, Y. C. Kim, R. Ghirlando, L. F. Saidi, G. Hummer, and J. H. Hurley, “Hybrid Structural Model of the Complete Human ESCRT-0 Complex,” *Structure*, 17, 3, 406–416, **2009**.

[52] A. Hierro, J. Sun, A. S. Rusnak, J. Kim, G. Prag, S. D. Emr, and J. H. Hurley, “Structure of the ESCRT-II endosomal trafficking complex,” *Nature*, 431, 7005, 221–225, **2004**.

[53] D. Schley, R. J. Whittaker, and B. W. Neuman, “Arenavirus budding resulting from viral-protein-associated cell membrane curvature,” *J. Royal Soc. Interface*, 10, 86, p. 20130403, **2013**.

[54] C. Raiborg, J. Wesche, L. Malerod, and H. Stenmark, “Flat clathrin coats on endosomes mediate degradative protein sorting by scaffolding Hrs in dynamic microdomains,” *J. Cell Sci.*, 119, 12, 2414–2424, **2006**.

[55] N. S. Gov, “Guided by curvature: shaping cells by coupling curved membrane proteins and cytoskeletal forces,” *Philos. Trans. Royal Soc. B*, 373, 1747, p. 20170115, **2018**.

[56] J. Derganc and A. Copic, “Membrane bending by protein crowding is affected by protein lateral confinement,” *Biochimica Et Biophysica Acta-biomembranes*, 1858, 6, 1152–1159, **2016**.

[57] J. C. Stachowiak, E. M. Schmid, C. J. Ryan, H. S. Ann, D. Y. Sasaki, M. B. Sherman, P. L. Geissler, D. A. Fletcher, and C. C. Hayden, “Membrane bending by protein-protein crowding,” *Nature Cell Biology*, 14, 9, 944–+, **2012**.

[58] E. Szymanska, N. Budick-Harmelin, and M. Miaczynska, “Endosomal ”sort” of signaling control: The role of ESCRT machinery in regulation of receptor-mediated signaling pathways,” *Semin. Cell Dev. Biol.*, 74, 11–20, **Feb. 2018**.

[59] A. Roux, D. Cuvelier, P. Nassoy, J. Prost, P. Bassereau, and B. Goud, "Role of curvature and phase transition in lipid sorting and fission of membrane tubules," *Embo Journal*, 24, 8, 1537–1545, **2005**.

[60] T. Baumgart, S. T. Hess, and W. W. Webb, "Imaging coexisting fluid domains in biomembrane models coupling curvature and line tension," *Nature*, 425, 6960, 821–824, **2003**.

[61] J. M. Allain, C. Storm, A. Roux, M. B. Amar, and J. F. Joanny, "Fission of a multiphase membrane tube," *Physical Review Letters*, 93, 15, p. 158104, **2004**.

[62] H. Lodish, A. Berk, P. Matsudaira, C. Kaiser, M. Krieger, M. Scott, L. Zipursky, and J. Darnell, *Molecular Cell Biology, Fifth Edition*, 2000, ch. Chemical Building Blocks of Cells, 30–37.

[63] M. S. Kostelansky, J. Sun, S. H. Lee, J. Kim, R. Ghirlando, A. Hierro, S. D. Emr, and J. H. Hurley, "Structural and functional organization of the ESCRT-I trafficking complex," *Cell*, 125, 1, 113–126, **2006**.

[64] R. Lipowsky, "Coupling of bending and stretching deformations in vesicle membranes," *Adv. Colloid Interface Sci.*, 208, 14–24, **2014**.

[65] M. P. do Carmo, *Differential Geometry of Curves and Surfaces.* Prentice-Hall, Inc., Englewood Cliffs, New Jersey, 1976.

[66] F. Julicher and R. Lipowsky, "Shape transformations of vesicles with intramembrane domains," *Phys. Rev. E*, 53, 3, 2670–2683, **1996**.

[67] T. Wollert, C. Wunder, J. Lippincott-Schwartz, and J. H. Hurley, "Membrane scission by the ESCRT-III complex," *Nature*, 458, 7235, 172–U2, **2009**.

[68] D. S. Johnson, M. Bleck, and S. M. Simon, "Timing of ESCRT-III protein recruitment and membrane scission during HIV-1 assembly," *Elife*, 7, p. e36221, **2018**.

[69] A. J. Pak, J. M. A. Grime, P. Sengupta, A. K. Chen, A. E. P. Durumeric, A. Srivastava, M. Yeager, J. A. G. Briggs, J. Lippincott-Schwartz, and G. A. Voth, "Immature HIV-1 lattice assembly dynamics are regulated by scaffolding from nucleic acid and the plasma membrane," *Proc Natl Acad Sci U S A*, 114, 47, E10 056–E10 065, **2017**.

[70] E. Jones, T. Oliphant, P. Peterson *et al.*, "SciPy: Open source scientific tools for Python," **2001**. [Online]. Available: http://www.scipy.org/

[71] R. Lipowsky, "Budding of Membranes Induced by Intramembrane Domains," *J Phys II*, 2, 10, 1825–1840, **1992**.

Supplementary information

Endocytic Pathway

In Fig. 6 the role of ILVs within the endocytic pathway is shown schematically.

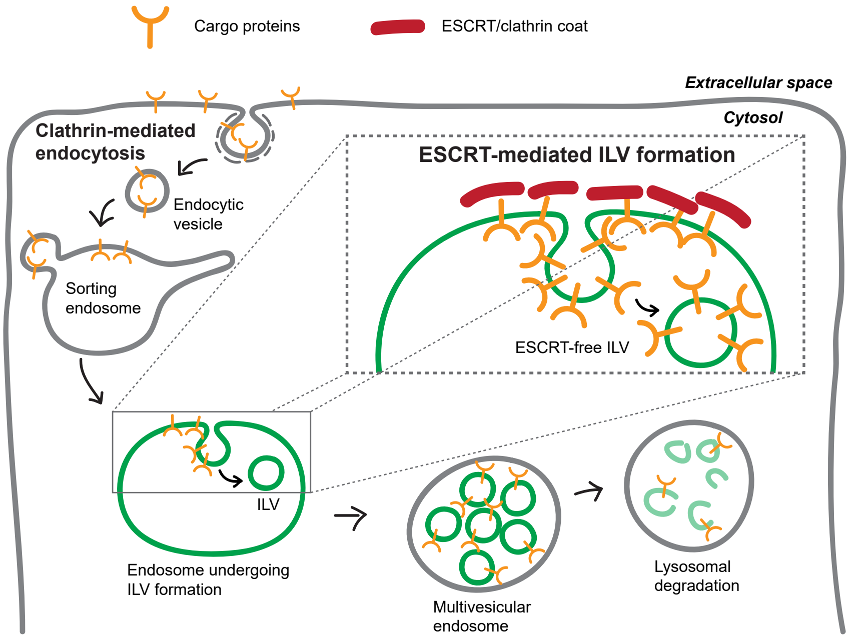

Figure 6: Endocytic pathway Transmembrane proteins (cargo), for example activated growth factor receptors, can enter the degradative endocytic pathway via endocytosis. To allow degradation in the lysosomes by lysosomal digestive enzymes, the cargo needs to be internalized into intraluminal vesicles (ILVs). Cargo sorting and the formation of ILVs is mediated by the ESCRT machinery, giving rise to multivesicular endosomes.

Energy Barrier

For a diffusive process in one-dimension in a harmonic potential E of the form $E(x) = 4\Delta E_\mathrm{B}\frac{x}{L}\left(1-\frac{x}{L}\right)$, with the energy barrier E_B, the diffusion coordinate x and the maximal value of the diffusion coordinate L, Kim et al. derived the following expressions for the transition path time τ_d, *i.e.* the time to cross the barrier if the process starts at x=0 and does not return to x=0, and the waiting time τ_wt, *i.e.* the mean time to cross the barrier, when starting from x=0, where the process may return to x=0 multiple times [47]:

$$\tau_\mathrm{d} \approx \begin{cases} \frac{L^2}{D}\left[\frac{1}{6}-\frac{2}{45}\frac{\Delta E_\mathrm{B}}{k_\mathrm{B}T}\right], & \frac{\Delta E_\mathrm{B}}{k_\mathrm{B}T} \ll 1 \\ \frac{L^2}{D}\frac{\ln\left(2e^{\gamma_e}\frac{\Delta E_\mathrm{B}}{k_\mathrm{B}T}\right)}{8\frac{\Delta E_\mathrm{B}}{k_\mathrm{B}T}}, \text{with } \gamma_e \approx 0.577 \text{ the Euler gamma constant} & \frac{\Delta E_\mathrm{B}}{k_\mathrm{B}T} \gg 1 \end{cases} . \tag{13}$$

$$\tau_\mathrm{wt} = \frac{L^2}{D}\frac{\pi \mathrm{erf}(\sqrt{\Delta \mathrm{E_B}/\mathrm{k_BT}})\mathrm{erfi}(\sqrt{\Delta \mathrm{E_B}/\mathrm{k_BT}})}{8\Delta E_\mathrm{B}/k_\mathrm{B}T} \tag{14}$$

Here, D is the diffusion constant. Eq. 13 and Eq. 14 show that the ratio $\tau_\mathrm{d}/\tau_\mathrm{wt}$ only depends on the energy barrier ΔE_B. Fig. 7 shows the ratio $\tau_\mathrm{d}/\tau_\mathrm{wt}$ as a function of the energy barrier. For a small energy barrier the curve approaches as value of $\tau_\mathrm{d}/\tau_\mathrm{wt}$=1/3. The experimentally obtained value for the transition path time and the mean first passage time are: τ_{d}=(161±94)s, τ_{wt}(203±47)s [15], with leads to a ratio 0.3$\leq$ $\tau_{\mathrm{d}}/\tau_{\mathrm{wt}}$ $\leq$1.6 (indicated as gray shaded are in Fig. 7). Hence the upper limit exceeds the maximal theoretical value of 1/3, which we attribute to the shape of the energy landscape, which is not a perfectly harmonic potential for the case is ILV formation. Within the limit of the experimental uncertainty, we obtain an upper limit for the energy barrier of $\Delta E_{\mathrm{B}} \approx 0.6 \mathrm{k_B T}$.

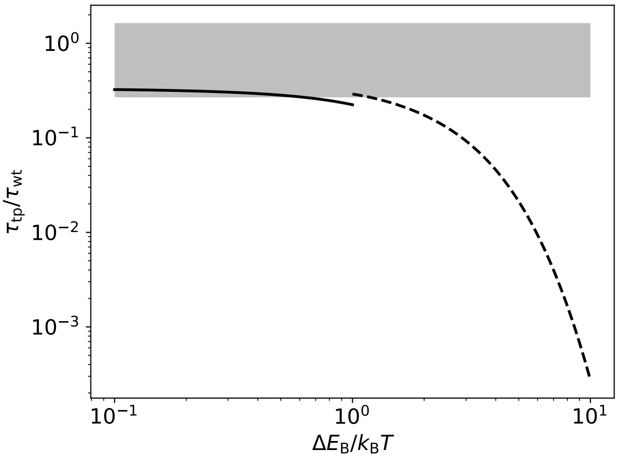

Figure 7: Energy barrier The ratio of transition path time and waiting time in dependence of the energy barrier ΔE_{B} (Eq. 13 solid line, Eq. 14 dashed line). The range of experimental values is indicated as gray shaded area.

Mean and Gaussian Curvature

A key assumption in our theoretical model is that ESCRTs induce a concentration dependent Gaussian bending rigidity. The membrane energy therefore depends on the mean curvature as well as on the Gaussian curvature. To gain a better understand on how mean and Gaussian curvature proceed along the membrane shape, as the membrane transitions from a flat surface to a spherical vesicle, Fig. 8 shows both curvatures for three exemplary membrane shapes. The same shapes are shown in Fig. 3a in the main text.

We rescale both mean and Gaussian curvature with the ILV curvature C_{g}:

$$\text{Mean curvature: } \kappa_{\mathrm{m}} = \frac{\frac{d\psi}{dS} + \frac{\sin\psi}{R}}{2C_{\mathrm{g}}} \tag{15}$$

$$\text{Gaussian curvature: } \kappa_{\mathrm{g}} = \frac{\frac{d\psi}{dS}\frac{\sin\psi}{R}}{C_{\mathrm{g}}^2} \tag{16}$$

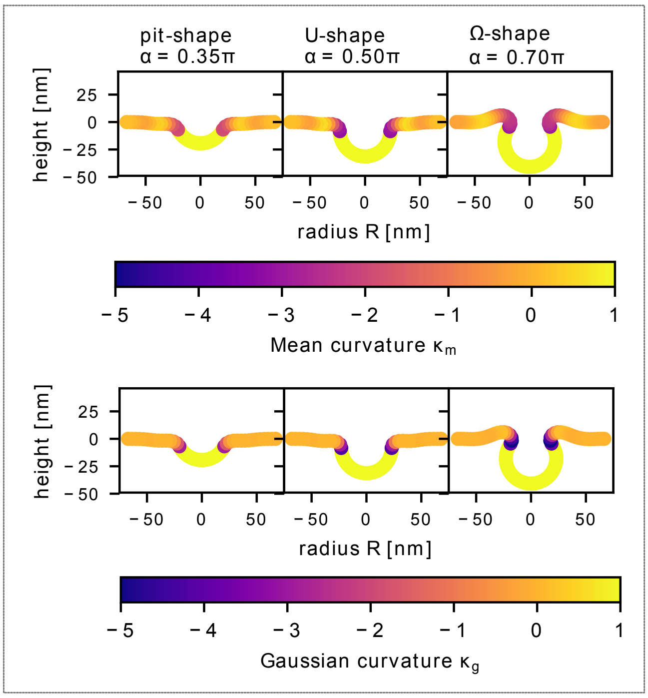

Figure 8: Mean and Gaussian Curvature The membrane shape is shown for different angles α, corresponding to the three categories: pit-shape ($\alpha = 0.35\pi$), U-shape ($\alpha = 0.5\pi$) and Ω-shape ($\alpha = 0.7\pi$). The top row shows the mean curvature along the membrane shapes. The bottom row shows the Gaussian curvature along the membrane shapes.

Simulation Method

The minimal energy shape of the outer region is obtained by parametrizing the angle ϕ as

$$\phi(s) = \alpha\left(1 - \frac{s}{s_{\text{end}}}\right) + \sum_{i=1}^{N} \phi_i \sin\left(i\pi\frac{s}{s_{\text{end}}}\right) \tag{17}$$

The prefactors ϕ_i are obtained by minimizing the energy Eq. 10 using the python *basinhopping* routine [70] with 100 iteration steps and an initial step size of 0.01.

To optimize the number of terms N, we perform an energy minimization considering only the bending energy Eq. 2. Evidently the energy is minimal and equal to zero, if the mean curvature is zero. Hence, a membrane only subjected to bending energy is a suitable test case to compare the numerically and the analytically obtained minimal energy shape.

In Fig. 9 the membrane shape of the outer membrane region is shown in dependence of the angle α for different N. As initial guess, we set the prefactors to ϕ_1=-1.6 and ϕ_i=0 for i >1. With increasing N the energy curve approaches the analytic result of E_κ=0. N=30 does not lead to a significant improvement compared to N=25. For numerical efficiency we hence chose N=25 for all simulations.

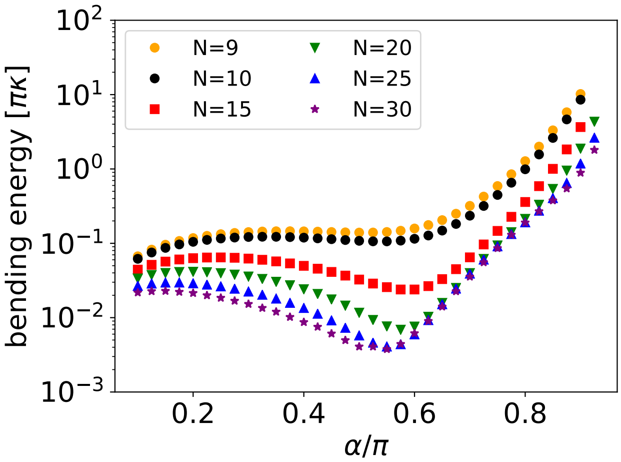

Figure 9: Bending Energy The numerically obtained bending energy of the outer membrane region. For a zero-mean-curvature shape the bending energy is zero, independent of the angles α.

For all N the numerically obtained bending energy deviates significantly from E_κ=0 as α approaches π. Hence, the bending energy is over estimated around $\alpha = \pi$. However, the energy curves investigated in the main text show a maximum for much smaller α, *i.e.* numerical error around $\alpha = \pi$ do not influence our findings reported in the main text.

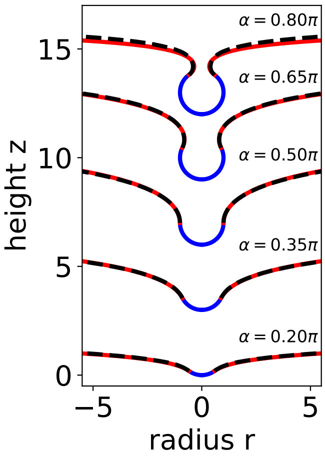

Figure 10: Membrane Shape Numerically obtained minimal energy shape (dashed, black line) and zero-mean-curvature shape (solid, red line). The shapes are shifted in z-direction for better visibility.

As a further test, we compare in Fig. 10 the numerically obtained minimal energy shape with a zero-mean-curvature shape for N=25 and different α, which shows good agreement. To determine the zero-mean-curvature shape we solve the following initial value problem with the python *odeint* routine [70]:

$$\frac{d\phi}{ds} = -\frac{\sin\phi}{r} \qquad \phi(0) = \alpha \tag{18}$$

$$\frac{dr}{ds} = \cos\phi \qquad r(0) = \sin\alpha \tag{19}$$

$$\frac{dz}{ds} = \sin\phi \qquad z(0) = 1 - \cos\alpha \tag{20}$$

The minimization of the full energy function Eq. 10 is performed in two steps. First, an energy minimization is performed considering only the bending energy. The thus obtained prefactors ϕ_i serve as an initial guess for the second step, where the full energy function is minimized.

Line Tension

A non-uniform protein density leads to an effective surface tension, which has an effect such that the density profile is flattened:

$$\Delta E_\lambda = 2\pi \int_0^\infty dS \lambda \left(\frac{d\rho}{dS}\right)^2 \approx 2\pi\lambda\rho_0 2 \left(\frac{C_1(S^*)C_2(S^*)}{C_\mathrm{g}}\right)^2 R(S^*) \tag{21}$$

Since the largest density gradient is found at the boundary between the protein coated and uncoated region, the term $\left(\frac{d\rho}{dS}\right)^2$ is well approximated by a delta-distribution around S^*, with S^* the arc length at the boundary of the coat-free vesicle. Hence, ΔE_λ acts like a line tension energy with an effective line tension $\lambda\rho_0^2$ that is scales by the Gaussian curvature at the boundary between coated and uncoated region. Mercker et al. estimated the line tension of ESCRT-proteins in the range of $\lambda\rho_0^2$ ≈0.005pN [40], which at about two orders of magnitude smaller than the typical line tension of lipid rafts [71]. Assuming this value for the line tension was motivated mainly by the observation that ECSRT-I and ESCRT-II do not form large clusters [13], which indicated a weak interaction among proteins.

To evaluate the impact of the line tension on the energy landscape, we write Eq. 21 in rescaled units as:

$$\frac{\Delta E_\lambda}{\pi\kappa} = \widetilde{\lambda}\left[r\left(c_1 c_2\right)^2\right]_{s=s^*}, \text{ with } \widetilde{\lambda} = \frac{2\lambda\rho_0^2}{C_\mathrm{g}\kappa} \tag{22}$$

and $c_1 = C_1/C_\mathrm{g}$, $c_2 = C_2/C_\mathrm{g}$. The rescaled radius at the boundary between coated and uncoated region is obtained analytically as $r(s^*) = \sin\alpha$, whereas the Gaussian curvature c_1c_2 is obtained from the energy minimization for $\widetilde{\lambda}$=0. This approximation serves as an upper limit of the energy term ΔE_λ. In Fig, 11 the total energy is shown in dependence of α for ϵ=2.0 and $\widetilde{\sigma}$=0.1. For a curvature of C_g=(23nm)$^{-1}$, a bending rigidity κ=10k$_\mathrm{B}$T [23] and a line tension $\lambda\rho_0^2$=0.005pN the rescaled line tension becomes $\widetilde{\lambda}$=0.006. Fig. 11 shows that the energy landscape is not significantly altered for $\widetilde{\lambda}$=0.006.

If we assume an effective line tension that is several orders of magnitude larger, the line tension hinders the formation of a vesicle, which seems counter intuitive at first, since the radius at the boundary between coated and uncoated region decreases as the membrane transforms from a U-shape to an Ω-shape. However, the line tension is scaled by the squared of the Gaussian curvature at $s = s^*$, which increases rapidly with increasing α as a consequence, the term $\widetilde{\lambda}\left[(c_1c_2)^2\right]_{s=s^*}$ opposes neck closure.

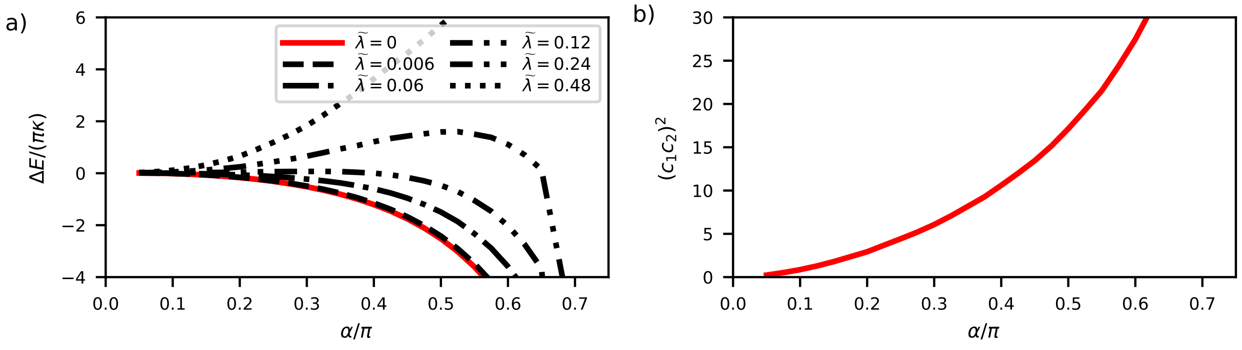

Figure 11: Line tension a) Energy (Eq. 10 main text and Eq. 22) for ϵ=2.0 and $\widetilde{\sigma}$=0.1 and different $\widetilde{\lambda}$. b) Squared rescaled Gaussian curvature at the boundary between coated and uncoated region.